Near-Infrared Squaraine Dye Encapsulated Micelles for *in Vivo* Fluorescence and Photoacoustic Bimodal Imaging

Sivaramapanicker Sreejith,[†] James Joseph,[†] Manjing Lin,[‡] Nishanth Venugopal Menon,[§] Parijat Borah,[†] Hao Jun Ng,[†] Yun Xian Loong,[†] Yuejun Kang,[§] Sidney Wing-Kwong Yu,[⊥] and Yanli Zhao*[,†,#]

[†]Division of Chemistry and Biological Chemistry, School of Physical and Mathematical Sciences, Nanyang Technological University, 21 Nanyang Link, 637371, Singapore, [‡]SingHealth Experimental Medicine Centre, Singapore Health Services Pte. Ltd., 20 College Road, 169856, Singapore, [§]School of Chemical and Biomedical Engineering, Nanyang Technological University, 62 Nanyang Drive, 637459, Singapore, [⊥]Department of Nuclear Medicine & PET, Singapore General Hospital, Outram Road, 169608, Singapore, and [#]School of Materials Science and Engineering, Nanyang Technological University, 639798, Singapore

ABSTRACT Combined near-infrared (NIR) fluorescence and photoacoustic imaging techniques present promising capabilities for noninvasive visualization of biological structures. Development of bimodal noninvasive optical imaging approaches by combining NIR fluorescence and photoacoustic tomography demands suitable NIR-active exogenous contrast agents. If the aggregation and photobleaching are prevented, squaraine dyes are ideal candidates for fluorescence and photoacoustic imaging. Herein, we report rational selection, preparation, and micelle encapsulation of an NIR-absorbing squaraine dye (D1) for *in vivo* fluorescence and photoacoustic bimodal imaging. D1 was encapsulated inside micelles constructed from a biocompatible nonionic surfactant (Pluoronic F-127) to obtain D1-encapsulated micelles ($D1_{micelle}$) in aqueous conditions. The micelle encapsulation retains both the photophysical features and chemical stability of D1. $D1_{micelle}$ exhibits high photostability and low cytotoxicity in biological conditions. Unique properties of $D1_{micelle}$ in the NIR window of 800−900 nm enable the development of a squaraine-based exogenous contrast agent for fluorescence and photoacoustic bimodal imaging above 820 nm. *In vivo* imaging using $D1_{micelle}$, as demonstrated by fluorescence and photoacoustic tomography experiments in live mice, shows contrast-enhanced deep tissue imaging capability. The usage of $D1_{micelle}$ proven by preclinical experiments in rodents reveals its excellent applicability for NIR fluorescence and photoacoustic bimodal imaging.

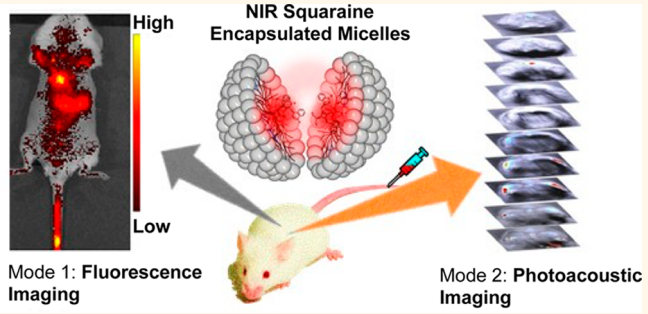

KEYWORDS: bioimaging · fluorescence tomography · micelles · photoacoustic tomography · squaraine dye

Novel optical imaging techniques, such as photoacoustic tomography (PAT), and their capabilities to probe structural, functional, and molecular states of biological specimens have been widely investigated during the past decades, and some of them have been accepted for clinic usage.[1−3] On the other hand, the development of background-free optical imaging techniques that can provide images with rich optical contrast *in vivo* by capitalizing on selective photon absorption is of great significance in the field of biomedical research.[4] However, each single imaging modality suffers inherent limitations such as limited tissue penetration, low sensitivity, and failing to provide anatomy information precisely.[5] Multimodal combinations of imaging modalities are expected to compensate for inherent limitations of individual imaging modality and are thus emerging as an inevitable trend in the development of new imaging techniques.[6,7] In optical imaging, a potential imaging approach that could offer tremendous opportunities for future clinic applications is to blend the salient features of fluorescence imaging and PAT at near-infrared (NIR) excitation.[8,9] Given the unique capabilities of such emerging multimodal imaging combinations, the design and development of new multimodal contrast agents in the NIR

* Address correspondence to zhaoyanli@ntu.edu.sg.

Received for review October 1, 2014 and accepted May 29, 2015.

Published online May 29, 2015
10.1021/acsnano.5b02172

region are greatly expected.[10−12] However, the design of NIR contrast agents that can be used in conjugation with these multimodal noninvasive optical imaging modalities remains challenging.[13−15] An ideal contrast agent for NIR fluorescence and photoacoustic imaging should typically offer excellent NIR fluorescence emissions and intense absorption along with good photochemical stability and low cytotoxicity in aqueous and biological conditions.[16,17] As a promising class of NIR dyes, squaraines have proven their versatility in a wide range of imaging applications.[18−22] In this context, the selection of squaraines as bimodal contrast agents for NIR fluorescence and photoacoustic imaging is justified, since they possess excellent chemical and photophysical properties in the NIR region.

The main challenge that prevents the effective use of NIR properties of squaraine dyes relies on their ease of formation of aggregates in aqueous/biological conditions.[23] Thus, researchers have introduced new strategies to control their self-assembly, thereby enabling the efficient use of squaraines for various biological applications.[24−26] Recently, a new type of modified dicyanovinyl-substituted squaraines was reported and their photophysical properties were studied.[27−29] The substituted dicyanovinyl squaraine core allows for efficient tuning of NIR properties in the first NIR window. On the other hand, the encapsulation of squaraine dyes within micelles for multiphoton fluorescence bioimaging was established.[30] Therefore, a rational selection of a squaraine derivative in conjugation with micelle-encapsulated protection strategy en route to the development of a new class of bimodal exogenous contrast agents for fluorescence and photoacoustic bimodal imaging in the first NIR window of 650−950 nm is of great importance.

Herein, we report the preparation of a new 4-methylquinolium-based dicyanovinyl-substituted squaraine with oxyethylene side chains (D1) and the encapsulation of D1 inside micelles constructed from a biocompatible nonionic surfactant (Pluronic F-127) to afford squaraine-encapsulated micelle $D1_{micelle}$ (Figure 1). It was observed that the as-synthesized $D1_{micelle}$ exhibits high chemical stability and low cytotoxicity and could retain photophysical properties of D1 in the NIR region. The promising potential of $D1_{micelle}$ for *in vivo* NIR fluorescence and photoacoustic bimodal imaging was then demonstrated. Based on a literature survey as shown in Table S1 of the Supporting Information, the present work using a squaraine-encapsulated micelle ($D1_{micelle}$) is the first example of such kind, demonstrating an excellent bimodal imaging capability at 840 nm.

RESULTS AND DISCUSSION

D1 with oxyethylene side chains was synthesized based on previous literature reports with some modifications.[27,31] Condensation of dicyanovinyl-substituted squaric acid with two equivalents of *N*-glycolated

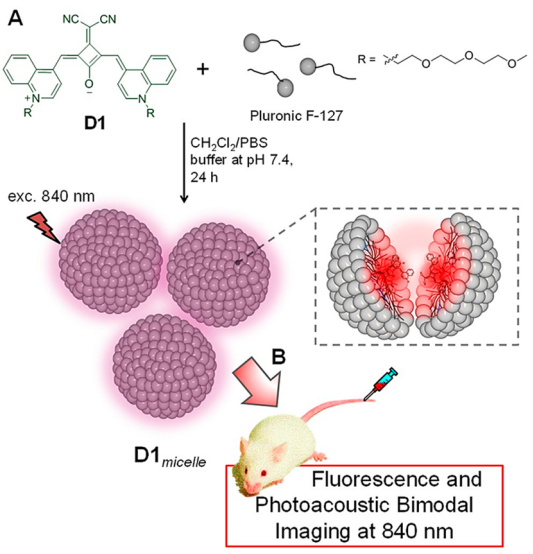

Figure 1. Schematic preparation of $D1_{micelle}$ for fluorescence and photoacoustic bimodal imaging. (A) Scheme showing the preparation of $D1_{micelle}$ and a single micelle containing D1. (B) Scheme showing intravenous injection of $D1_{micelle}$ for fluorescence and photoacoustic bimodal imaging in a mouse.

4-methylquinolium iodide in a 1:1 azeotropic mixture of benzene and *n*-butanol afforded D1 in 9−10% yield. As-synthesized dye was then characterized by NMR and high-resolution mass spectrometry (see the Supporting Information for more synthesis and characterization details). The photophysical properties of D1 were investigated in dimethyl sulfoxide (DMSO). D1 (1×10^{-4} M) in DMSO exhibits intense absorption at 867 nm and emission at 907 nm with a Stoke shift of 40 nm (Figure 2a,b). The inset of Figure 2b shows the false-color pixel intensity map corresponding to the emission of D1 in DMSO at room temperature.

The absorption spectra of D1 in DMSO show a significant blue shift followed by bleaching of optical properties upon increasing the water content from 0 to 90%. Figure 2c reveals the changes in the absorption spectra of D1 in DMSO upon the addition of water, indicating the feasibility of rapid aggregate formation (*H*-aggregate) of D1 in aqueous conditions.[23] The false-color pixel intensity mapping also exhibits a significant emission quenching in water, which further confirms the formation of aggregates *in situ* (Figure 2d). In order to preserve the photophysical properties and stability of D1 in aqueous conditions, we adopted the micelle encapsulation strategy for further studies.

The micelle encapsulation of D1 was carried out in a dichoromethane/phosphate-buffered saline (PBS) mixture by following previously reported procedures (see the Methods section for experimental details).[32,33] In our study, we selected poloxamer 407, a biocompatible polymer commonly known as Pluronic F-127 (PF-127),[34] for the micelle fabrication. PF-127 has been approved by the U.S. Food and Drug Administration (FDA) and studied extensively for sustained delivery of

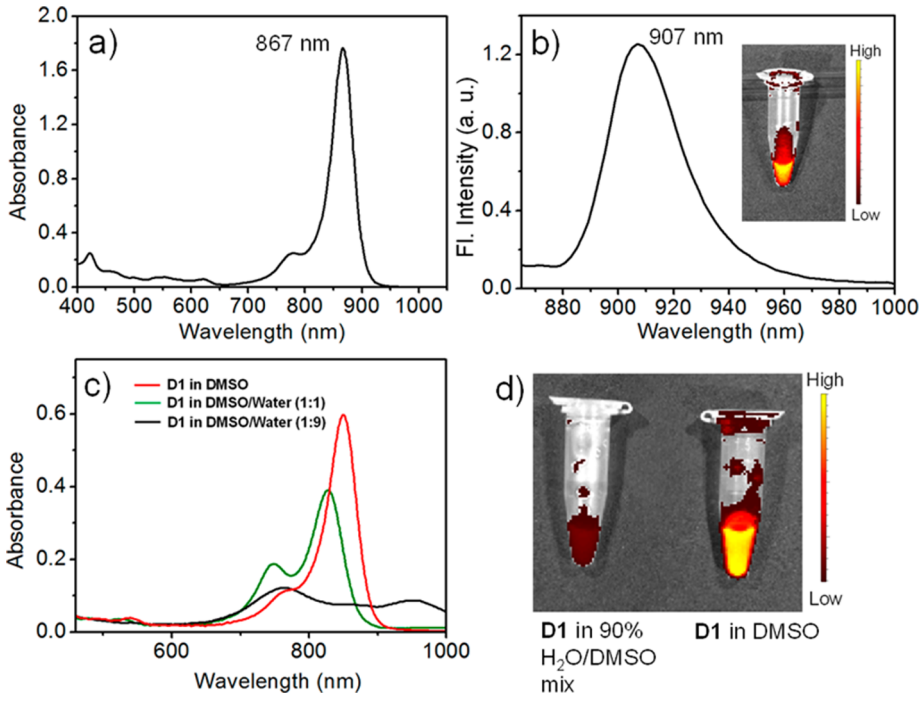

Figure 2. Photophysical properties of D1. (a) UV/vis absorption spectrum and (b) emission spectrum (excited at 840 nm) of D1 in DMSO (1×10^{-4} M). Inset of (b) shows fluorescence of D1 in DMSO as false-color pixel intensity. (c) Changes in the absorption spectra of D1 in DMSO (1×10^{-4} M) upon increasing content of water from 0 to 90%. (d) False-color pixel intensity map showing fluorescence images of D1 in DMSO and a 90% water/DMSO mixture under 800 nm excitation.

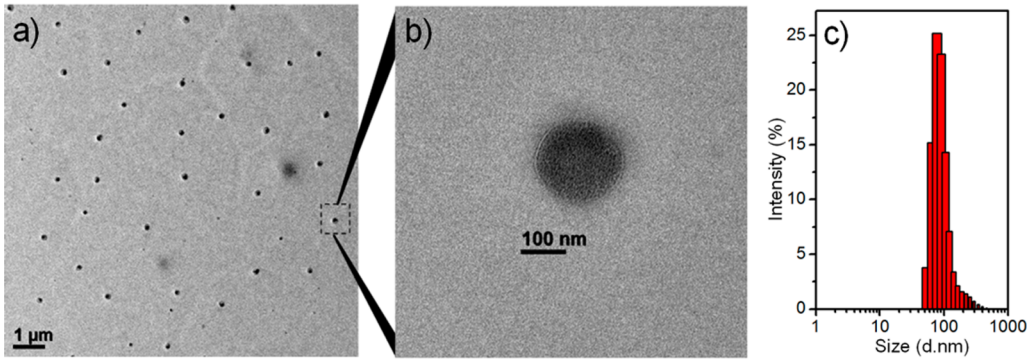

Figure 3. (a) TEM image of $D1_{micelle}$ in water and (b) high-magnification TEM image of a single $D1_{micelle}$ particle. (c) Dynamic light scattering data showing the hydrodynamic size of $D1_{micelle}$ in PBS buffer at pH 7.4.

pharmaceutical active ingredients.[35,36] After the preparation of $D1_{micelle}$, it was characterized by transmission electron microscope (TEM) and dynamic light scattering (DLS) techniques. Figure 3a shows the TEM image of $D1_{micelle}$ in PBS buffer. The TEM analysis reveals uniform spherical micelle formation with a good contrast. Apparently, the presence of organic dye inside the micelle enhances the visibility of spherical morphology during TEM analysis. A high-resolution TEM image (Figure 3b) of a single $D1_{micelle}$ particle clearly indicates the formation of micelles with an average diameter of 100 ± 30 nm. Furthermore, DLS measurement (Figure 3c) shows a hydrodynamic diameter of 184 ± 30 nm with a narrow size distribution for $D1_{micelle}$, which is consistent with the observation from TEM images.

We then investigated the optical properties, the effect of nucleophiles, and the stability of $D1_{micelle}$ in biological fluids. The effect of pH on the photophysical properties of $D1_{micelle}$ in comparison with D1 alone was also studied. The UV/vis absorption spectrum of $D1_{micelle}$ in PBS at pH 7.4 exhibits broad absorption ranging from 800 to 900 nm with the maximum absorbance at 840 nm corresponding to the encapsulated D1 (Figure 4a). This monomeric existence of D1 inside micelles demonstrates successful preservation of its optical characteristics in completely aqueous conditions. The absorption band below 700 nm may be due to the scattering from $D1_{micelle}$. Figure 4b shows the fluorescence spectrum of $D1_{micelle}$ in PBS at pH 7.4. A blue shift in the emission maximum was observed in aqueous solution, which was a common phenomenon

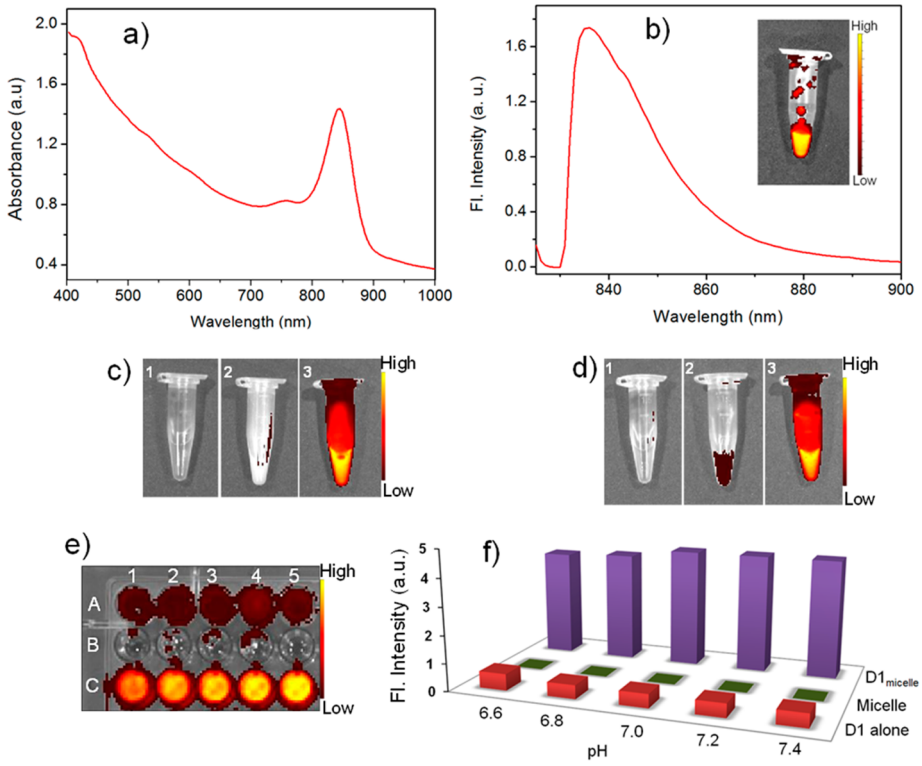

Figure 4. (a) UV/vis absorption and (b) fluorescence emission spectra of $D1_{micelle}$ in PBS buffer at pH 7.4. Inset of panel b shows false-color pixel intensity image corresponding to fluorescence of $D1_{micelle}$ at 840 nm (λ_{ex} 745/30 nm). (c, d) False-color pixel intensity images showing the stability of D1 and $D1_{micelle}$: (c1) HBP alone, (c2) D1 (1×10^{-4} M) in HBP, and (c3) $D1_{micelle}$ in HBP; (d1) BSA alone, (d2) D1 (1×10^{-4} M) in BSA, and (d3) $D1_{micelle}$ in BSA. (e) Fluorescence mapping image of a portion of a 96-well plate showing the pH effect on D1 (A1−A5), micelle alone (B1−B5), and $D1_{micelle}$ (C1−C5). (f) Plot showing the variation of fluorescence intensity *versus* pH (pH range of 6.6−7.4) for D1 (red bars), micelle alone (green bars), and $D1_{micelle}$ (purple bars).

attributed to the existence of D1 in a nonpolar microenvironment inside the micelle.[30,32] A fluorescence false-color pixel intensity mapping of $D1_{micelle}$ shows intense emission at 840 nm in PBS buffer at pH 7.4 (Figure 4b, inset).

Indocyanine green (ICG) is a commonly used biocompatible dye as a contrast agent in various imaging modalities. We compared the photophysical properties of $D1_{micelle}$ with ICG in water in order to prove the significance of the micelle encapsulation strategy. ICG exhibits a broader absorption spectrum with a maximum peak at 810 nm in PBS at pH 7.4. The spectral signature of $D1_{micelle}$ shows absorption in the visible and NIR regions with a maximum intensity at 840 nm (Figure S1a in the Supporting Information). Compared to ICG, $D1_{micelle}$ exhibits a 30 nm red shift in the absorption maximum, which indicates its increase in the effective range of analysis. Figure S1b in the Supporting Information shows a comparison of concentration-dependent fluorescence mapping of a microwell plate with $D1_{micelle}$ (A1−A5) and ICG (B1−B5) in PBS at pH 7.4. It is evident that $D1_{micelle}$ exhibits intense fluorescence intensities in buffered aqueous conditions at concentrations ranging from 10 to 0.6 μM. Thus, the potential capability of $D1_{micelle}$ for fluorescence imaging was proven as compared to a known standard dye.

D1 in the presence of a nucleophile such as cysteine undergoes an addition reaction, thereby bleaching all its photophysical properties (Figure S2a in the Supporting Information).[37,38] However, $D1_{micelle}$ shows no changes in the absorption maximum at 840 nm, which indicates the immunity of $D1_{micelle}$ toward cysteine addition even at higher concentrations (Figure S2b in the Supporting Information). The photophysical stability of D1 (1×10^{-4} M) and $D1_{micelle}$ in biological fluids was then investigated by incubating them in human blood plasma (HBP) and bovine serum albumin (BSA) at 37 °C for 1 h. Fluorescence mapping (λ_{em} 840 nm, λ_{ex} 745/30 nm) was then carried out. Figure 4c shows the fluorescence false-color pixel intensity mapping of HBP after 1 h incubation with D1 and $D1_{micelle}$ at 37 °C, respectively. D1 underwent aggregation in HBP, which was indicated by visible precipitation in HBP. On the other hand, $D1_{micelle}$ was found to be stable, and its fluorescence was retained in HBP, which was obviously evident from the fluorescence intensity map. The stability of D1 and $D1_{micelle}$ was also investigated in BSA solution, and similar phenomena to the case in HBP were observed. Figure 4d shows the corresponding fluorescence mapping images. Furthermore, the pH effect on the stability and photophysical properties of D1, micelle alone, and $D1_{micelle}$ was studied in the pH range 6.6−7.4. Figure 4e shows the false-color

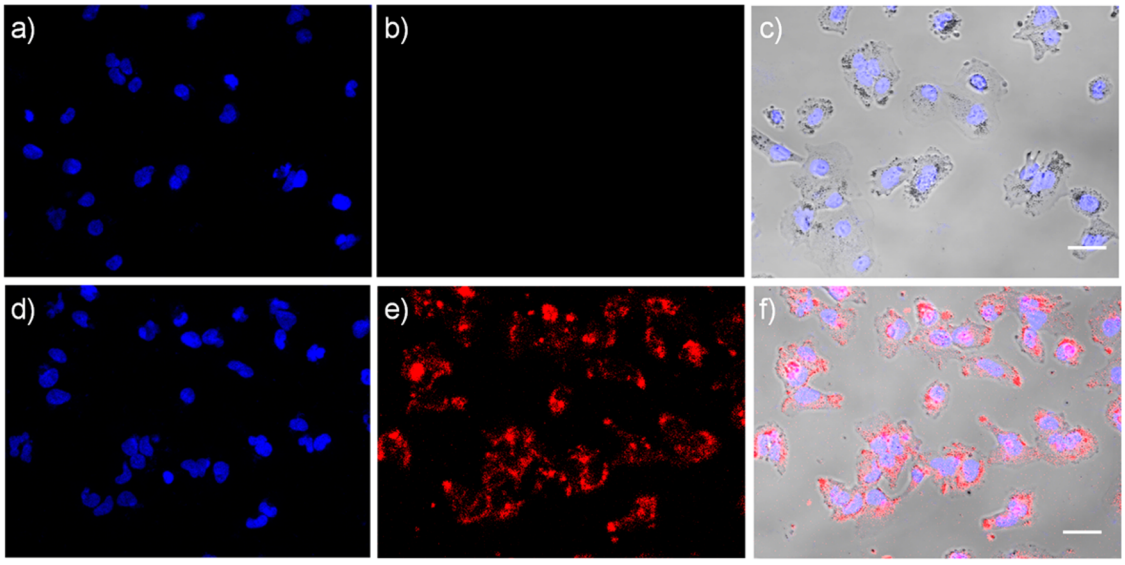

Figure 5. Fluorescence microscope images of the Huh-7 cell line incubated with (a−c) D1 and (d−f) $D1_{micelle}$ (10 μM) for 12 h. Florescence images of cells incubated with D1: (a) cell nuclei were stained with DAPI (excitation at 405 nm, DAPI channel), (b) emission at 820−850 nm obtained by exciting at 808 nm, and (c) overlay image of a and b. Florescence images of cells incubated with $D1_{micelle}$: (d) DAPI channel (excitation at 405 nm), (e) emission at 820−850 nm obtained by exciting at 808 nm, and (f) overlay image of d and e. Scale bar: 20 μM.

fluorescence mapping image (λ_{em} 840 nm) of a 96-well plate section filled with D1 (A1−5), micelle alone (B1−5), and $D1_{micelle}$ (C1−5) in the pH range 6.6−7.4 (from no. 1 to no. 5 plate). Intense fluorescence at 840 nm was observed from $D1_{micelle}$ in comparison with D1 and micelle without the dye. Figure 4f shows a summary of fluorescence intensity variation based on Figure 4e. Thus, the high stability of D1 inside the micelle ($D1_{micelle}$) at different pH's is evident from the comparison plot of fluorescence intensity at 840 nm.

The inherent cytotoxicity of $D1_{micelle}$ was evaluated using the MTT (3-(4,5-dimethylthiazolyl-2)-2,5-diphenyltetrazolium bromide) viability assay with the human hepatoma cell line (Huh-7) incubated for 24 h. The cell viability was measured by varying the concentrations of $D1_{micelle}$ in the micromolar range. A summary of the viability assay is shown in Figure S3 of the Supporting Information, which clearly indicates that $D1_{micelle}$ has no considerable cytotoxicity at low to moderate concentrations. The low cytotoxicity and good solubility in aqueous conditions as well as retained NIR photophysical properties encouraged us to further investigate the imaging capability of $D1_{micelle}$ both *in vitro* and *in vivo*.

The *in vitro* fluorescence imaging capability of $D1_{micelle}$ was assessed in comparison with D1 alone by NIR fluorescence imaging in the Huh-7 cell line. Aqueous solutions of D1 alone and $D1_{micelle}$ were incubated separately with Huh-7 cells for 12 h and were then imaged under 808 nm excitation. Figure 5 shows the fluorescence microscopy images of Huh-7 cells (40× objective) treated with D1 alone and $D1_{micelle}$, respectively. The blue fluorescence from the cell nucleus stained with 4′,6-diamidino-2-phenylindole (DAPI) can be observed in Figure 5a,d. The cells incubated with D1 alone show no emission fluorescence collected at 820−850 nm (Figure 5b and overlay image Figure 5c) upon excitation at 808 nm, indicating a failed endocytosis or aggregation of D1 in cellular environments. Huh-7 cells incubated with $D1_{micelle}$ clearly show high fluorescence intensity at 820−850 nm with a complete distribution in the cytoplasm of the cells. Figure 5e and f are the fluorescence images of the cells incubated with $D1_{micelle}$. Together with the low cytotoxicity obtained from the MTT assay and the fluorescence imaging experiments, the promising potential of $D1_{micelle}$ for *in vitro* fluorescence bioimaging was successfully proven.

In vivo fluorescence imaging was then carried out using a live 7-week-old severe combined immune deficiency (SCID) female mouse. Belly fur was removed using a depilatory cream prior to imaging. The *in vivo* fluorescence imaging studies on the mouse were performed using an IVIS lumina II preclinical imaging system and analyzed using IVIS Living Imaging 4.4. The animal was anesthetized with isoflurane, and the fluorescence images were acquired from the dorsal side of the mouse (see the Methods section for more details). Fluorescence imaging of the mouse placed in the supine position was performed in epifluorescence mode before and after the administration of $D1_{micelle}$. The same illumination and acquisition settings were used for all fluorescence image acquisitions. Figure 6a shows the fluorescence image of the mouse before the injection of $D1_{micelle}$. No detectable fluorescence signals were observed when imaged with 745/30 nm excitation and 840/20 nm emission settings. Then, $D1_{micelle}$ (200 μL) was injected intravenously, and the $D1_{micelle}$ concentration was calculated as 1.47×10^{-5} M per intravenous injection after optimizing four repeated

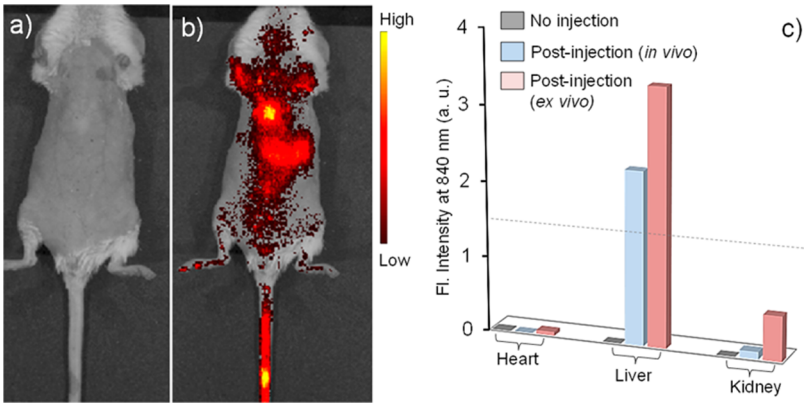

Figure 6. (a, b) Tracking of $D1_{micelle}$ distribution in a live mouse before and after intravenous injection using the IVIS imaging system. Fluorescence reflectance images from the dorsal side of a female mouse were measured (a) before and (b) after 2 min of intravenous injection with $D1_{micelle}$ (200 μL). (c) Quantitative fluorescence reflectance image analysis showing $D1_{micelle}$ distribution in the major organs (threshold intensity of 1.5×10^8 p/s/cm^2).

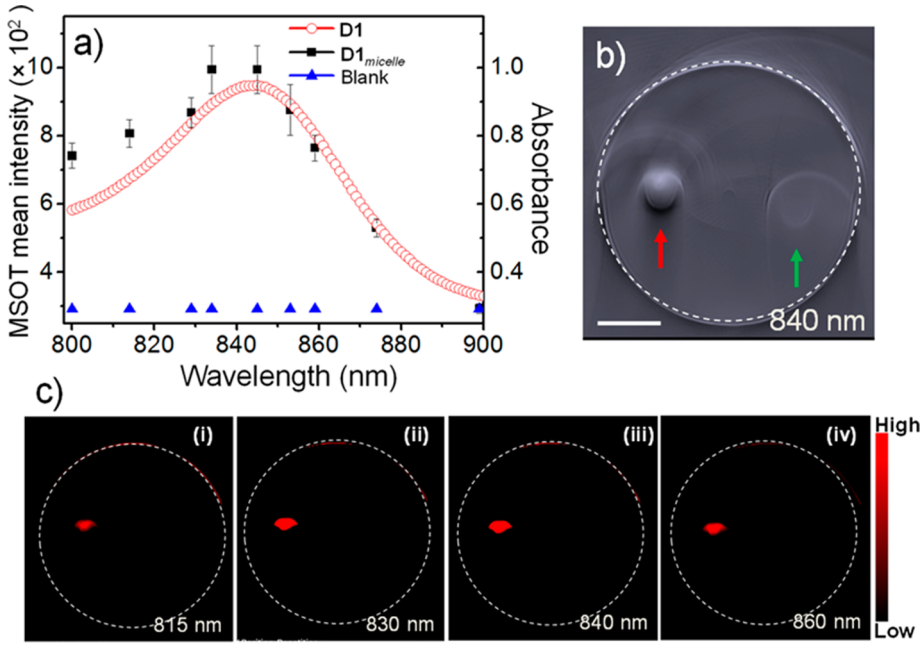

Figure 7. Multispectral photoacoustic imaging of a tissue-mimicking phantom containing $D1_{micelle}$. (a) Black squares and blue triangles represent multispectral photoacoustic mean intensity of $D1_{micelle}$ and the blank control (PBS at pH 7.4), respectively, inside a tissue-mimicking phantom. The red spectrum shows corresponding absorption of $D1_{micelle}$ in PBS at pH 7.4. (b) Single-wavelength photoacoustic image of a phantom acquired at 830 nm (scale bar: 3 mm). The red arrow and green arrow indicate the channels containing $D1_{micelle}$ and blank solution, respectively. (c) Spectrally resolved MSOT images of the $D1_{micelle}$ distribution in the phantom at an excitation wavelength of (i) 815, (ii) 830, (iii) 840, and (iv) 860 nm.

trials. The thoracic/abdominal area of the mouse was imaged within 35 min after the administration. Figure 6b presents the top view fluorescence image of the mouse at 840 nm excitation. After the imaging experiments, the mouse was euthanized, its organs were dissected, and the obtained sections were imaged. As evident from Figure 6c, the accumulation of $D1_{micelle}$ was primarily in the liver (2.4×10^8 p/s/cm^2 upon setting a threshold intensity of 1.5×10^8 p/s/cm^2). Figure S4 in the Supporting Information shows a photograph of the fluorescence reflectance image for the internal organs of mouse imaged at 840 nm. Clear localization of $D1_{micelle}$ in the liver (abdominal cavity) was observed, indicating the effective fluorescence tracing of $D1_{micelle}$ metabolism and accumulation. In short, *in vitro* and *in vivo* fluorescence imaging experiments demonstrate the high stability and potential of $D1_{micelle}$ as an NIR imaging probe for fluorescence microscopy and tomographic applications.

The photoacoustic imaging capability of $D1_{micelle}$ was initially studied using a tissue-mimicking phantom prior to *in vivo* imaging investigations. Photoacousic imaging studies were performed using the multispectral optoacoustic tomography (MSOT) system. Detailed descriptions of the imaging system and experimental parameters are given in the Methods section. A

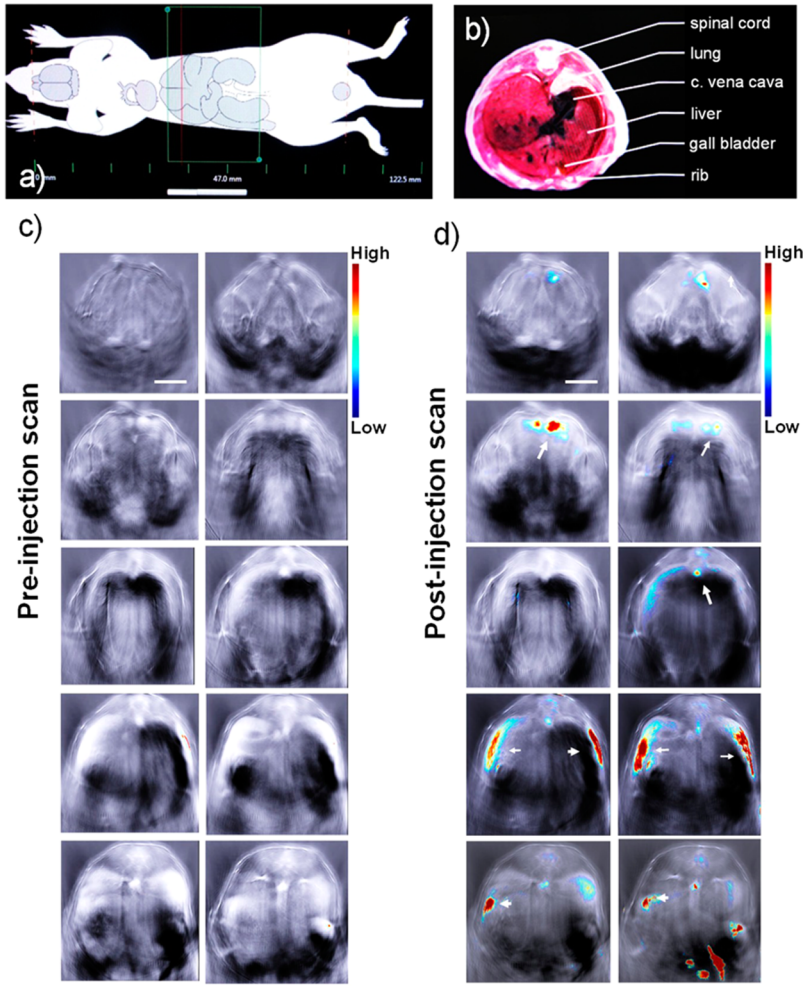

Figure 8. Single-wavelength photoacoustic images of live mouse anatomy at 840 nm. (a) Schematic diagram of completely scanned area. (b) Schematic section corresponding to a single area under analysis. (c) Individual anatomy sections of a live mouse before intravenous injection of $D1_{micelle}$ (scale bar: 6 mm). (d) Individual anatomy sections recorded after 35 min postintravenous injection of $D1_{micelle}$ (scale bar: 6 mm).

cylindrical tissue-mimicking phantom having a 4 mm diameter with two inclusions each was used to evaluate the photoacousic signal generation from $D1_{micelle}$. $D1_{micelle}$ in PBS buffer at pH 7.4 was loaded inside the first inclusion of the phantom, and the second inclusion containing the PBS buffer at pH 7.4 served as the control. Photoacoustic signals were then measured for excitation wavelengths ranging from 800 to 900 nm with 15 nm step intervals. Figure 7a displays the absorption spectrum (red dots) of $D1_{micelle}$ in PBS buffer at pH 7.4 along with corresponding photoacousic signal intensities for $D1_{micelle}$ (black squares) and control (blue triangles) across 800−900 nm. Multispectral scanning experiments show the maximum signal intensity in the range 815−840 nm, which indicate efficient photoacousic signal generation capability of $D1_{micelle}$ across these excitation wavelengths. Furthermore, the photoacousic signal intensities obtained from each excitation wavelength match well with the absorption spectrum of $D1_{micelle}$, indicating high photostability of $D1_{micelle}$ when used for photoacoustic studies. Figure 7b shows the corresponding photoacoustic image of a phantom loaded with $D1_{micelle}$ (red arrow) and blank control (PBS alone, green arrow). High signal intensity from $D1_{micelle}$ could be observed at 830 nm when compared to the control. Similarly, the photoacoustic images of the phantom at distinct excitation wavelengths from 800 to 900 nm were also generated (Figure 7c). The multispectral photoacoustic images show that the maximum image contrast is obtained at 830 nm, which in turn corresponds to the wavelength at which $D1_{micelle}$ exhibits the maximum absorbance. Thus, the photoacoustic image contrast varies linearly according to the absorption spectrum of $D1_{micelle}$.

To further investigate the *in vivo* photoacoustic imaging capability of $D1_{micelle}$, we carried out MSOT on an adult female mouse before and after intravenous injection of $D1_{micelle}$. Transverse slices of the mouse were formed by averaging photoacoustic signals acquired from 5 laser pulses for each excitation wavelength ranging from 800 to 900 nm with 15 nm step intervals. A tomographic view of 172° could be

achieved with the curvature of the detector containing a 64-element array transducer having a 5 MHz central frequency. During imaging, the mouse was translated across a distance of 150 mm with a 1 mm step size to form a transverse slice of the mouse at each position. Photoacoustic signals were acquired using a multichannel digitizer and then processed using standard machine integrated ViewMSOT software. Photoacoustic images were reconstructed using a model-based approach, and the photoacoustic signals from $D1_{micelle}$ were spectrally resolved using a principal component analysis (PCA)-based spectral unmixing technique. Images were acquired before (prescan) and after (postscan) intravenous (tail vein) injection of $D1_{micelle}$.

Figure 8 depicts spectrally resolved photoacoustic images (selected) at 840 nm wavelength from $D1_{micelle}$ within 35 min after the intravenous injection of $D1_{micelle}$. Schematic diagrams showing the scanned area and the anatomy of the section with the highest contrast are given in Figure 8a and b. No obvious contrast was observed for $D1_{micelle}$ during prescan (Figure 8c). Figure S5a in the Supporting Information shows the corresponding three-dimensional (3D) rendering of images during the prescan. A full set of images containing scans at 1 mm distance is provided in Figure S6 of the Supporting Information (also see Movie M1). After 35 min of $D1_{micelle}$ injection, a clear contrast difference could be visualized in the abdominal region (Figure 8d) for $D1_{micelle}$. Corresponding 3D rendering images are shown in Figure S5b of the Supporting Information. A full set of images containing scans at 1 mm distance is provided in Figure S7 of the Supporting Information (also see Movie M2). The obvious postinjection images provide solid evidence in favor of the photoacoustic imaging capability of $D1_{micelle}$ for *in vivo* imaging applications.

CONCLUSIONS

In summary, we have designed, synthesized, and characterized an NIR-active 4-methylquinolinium-based dicyanovinyl-substituted squaraine dye with oxyethylene side chains (D1). D1 was further encapsulated within micelles formed from a biocompatible nonionic surfactant (Pluronic F-127) to achieve $D1_{micelle}$. Easy aggregation of D1 in aqueous conditions was prevented *via* the micelle encapsulation strategy. Thus, $D1_{micelle}$ exhibited intense absorption and fluorescence properties from 800 to 900 nm in aqueous conditions with a maximum absorption at 840 nm. The low cytotoxicity, high stability in aqueous conditions, and reserved NIR photophysical properties make $D1_{micelle}$ an exceptional probe for fluorescence and photoacoustic bimodal imaging at 840 nm when compared to recently reported NIR probes (Table S1 in the Supporting Information). The *in vitro* and *in vivo* fluorescence imaging and *in vivo* photoacoustic imaging studies show that the developed $D1_{micelle}$ possesses tremendous capabilities for fluorescence and photoacoustic bimodal imaging.

In this work, we have successfully validated the strategy of micelle encapsulation in order to maintain the photophysical properties of a monomeric squaraine dye in aqueous conditions for *in vivo* fluorescence and photoacoustic bimodal imaging. This strategy could be generalized to other dye molecules having similar issues by selecting suitable encapsulation platforms. In the follow-up studies, we would like to incorporate targeting ligands within the dye-encapsulated micelles for targeted fluorescence and photoacoustic bimodal imaging. In this case, the dye-encapsulated micelles could be precisely localized in certain types of cells or organs for imaging. Such targeted imaging could guide the disease treatment, which is especially important for tumor therapy. Thus, the advanced development of the bimodal imaging system could be translated from mice to humans for clinical uses in the near future.

METHODS

All chemical reagents, unless otherwise specified, were purchased from Sigma-Aldrich Co. All solvents were of reagent grade and were purchased from local companies. All solvents were dried and distilled prior to use by following standard procedures. ^{1}H NMR spectra were recorded on a Bruker 300 MHz FT-NMR (model: Advance-DPX 300) spectrometer at 25 °C. The chemical shift (δ) data and coupling constant (J) values are given in parts per million (ppm) and hertz, respectively, unless otherwise mentioned. Electrospray ionization mass spectrometry (ESI-MS) measurements were carried out on a Waters QTof-Micro instrument. The high-resolution time-of-flight mass spectrometry (TOF-MS) was performed on a Waters Q-tof Premier MS spectrometer. Elemental analysis was performed on a EuroVector Euro EA elemental analyzer. UV/vis spectra were obtained by using a Shimadzu UV-3600 UV−vis−NIR spectrometer. Steady-state emission spectra at room temperature were obtained using a Shimadzu RF-5301PC spectrofluorimeter. Transmission electron microscopy (TEM) images were recorded on a JEM 1400 electron microscope (120 kV) equipped with slow scan CCD using cold cathode field emission as the gun. The samples were prepared by placing a droplet of the sample solution onto a TEM grid (copper grid, 300 mesh, coated with carbon film) and allowing it to air-dry. Dynamic light scattering measurements were carried out with a Zetasizer Nano ZS instrument from Malvern Instruments Ltd. at 298 K using a 633 nm "red" laser. The mean hydrodynamic size was calculated with Zetasizer software. Fluorescence tomography studies were performed using an IVIS Lumina II preclinical imaging system and analyzed using the IVIS Living Imaging 4.4 software (PerkinElmer Inc., Alameda, CA, USA). Photoacoustic imaging studies of the tissue-mimicking phantom and live mouse were performed using the MSOT system (MSOT Insight 64, iThera Medical GmbH).

Preparation of $D1_{micelle}$. In a typical experiment, D1 (1 mg mL^{-1}) and concentrated PF-127 surfactant (1.5×10^{-4} M) were dissolved in dicholormethane (10 mL) in an open round-bottom flask. An equal volume of PBS buffer at pH 7.4 was then added to

the mixture, which was allowed to stir at room temperature for 24 h. Complete evaporation of dichloromethane led to the formation of dye-encapsulated micelles ($D1_{micelle}$). As-prepared $D1_{micelle}$ was then filtered and dialyzed against water for 24 h in order to remove impurities and big particles.

***In Vitro* Cytotoxicity Assay.** The MTT assay test was carried out by following standard procedures. Huh-7 cells were seeded into a 96-well plate (1×10^4 cells per well) in DMEM (Dulbecco's modified Eagle's medium) cell culture medium containing 10% fetal bovine serum and grown under a humidified atmosphere with 5% CO_2 at 37 °C. After 12 h incubation, the media in the wells were replaced with fresh DMEM (100 μL per well) containing $D1_{micelle}$ with different concentrations, and the cells were further incubated for 6 h. Then, the medium was changed by DMEM (100 μL per well) containing MTT (0.5 mg mL^{-1}), followed by incubation for another 4 h. The culture medium was removed, and frozen crystals were dissolved with freshly prepared DMSO (100 μL). Before the cytotoxicity measurement, the plate was agitated gently for 15 min, and then the absorbance intensity at 560 nm was recorded by a microplate reader. The relative cell viability (%) for each sample related to the control well was finally calculated.

***In Vivo* Fluorescence Tomography.** *In vivo* fluorescence tomography studies of the live mouse were performed using an IVIS Lumina II preclinical imaging system and analyzed using the IVIS Living Imaging 4.4 software. A back-thinned back-illuminated CCD camera having 2048 × 2048 pixels cooled to −90 °C was used as the detector. Similar illumination and acquisition settings were used for acquiring all the fluorescence images. Images were acquired with binning factor 8, 4 s exposure time, and 12.9 cm field of view under 745/30 nm excitation and 840/20 nm emission filters. The mouse was then placed on a temperature-controlled stage inside the closed chamber of the imaging system equipped with an integrated isoflurane-based anesthesia system.

Multispectral Optoacoustic Studies. This study conforms to the Guide for the Care and Use of Laboratory Animals published by the National Institutes of Health, USA, and protocol approved by the Institutional Animal Care and Use Committee (IACUC), National University of Singapore. Photoacoustic imaging studies of the tissue-mimicking phantom and live mouse were performed using the MSOT system. The imaging system typically consists of an illumination source, a spherical array ultrasound probe, a parallel data acquisition system, and a computer. An optical parametric oscillator based laser, generating 5 ns duration pulses having an energy of 20 mJ and 10 Hz repetition rate, served as the illumination source. The output of the laser source could be tuned from 680 to 980 nm on a per pulse basis. The output beam of the laser was coupled into a fiber bundle and was guided onto the surface of the imaging sample. Photoacoustically generated volumetric data were detected using the 64-element piezoelectric transducer array having a spherical geometry, which can provide a tomographic view of 172°. Belly fur of the mouse was removed using depilatory cream prior to any imaging procedure. By following a previously explained anesthesia procedure, the animal was anesthetized and placed in a supine position over a thin polyethylene membrane, which was then positioned inside the imaging chamber filled with deionized water. The polyethylene membrane prevents the direct contact of the mouse with water and permits excellent acoustic coupling between the mouse and the detector array. The water bath was temperature controlled, and the mouse holder could be translated across the imaging plane to obtain multiple transverse image slices of the mouse. Photoacoustic images were acquired with an in-plane resolution of approximately 150 μm.

Conflict of Interest: The authors declare no competing financial interest.

Supporting Information Available: Additional experimental details. The Supporting Information is available free of charge on the ACS Publications website at DOI: 10.1021/acsnano.5b02172.

Acknowledgment. This research is supported by the National Research Foundation (NRF), Prime Minister's Office, Singapore, under its NRF Fellowship (NRF2009NRF-RF001-015) and Campus for Research Excellence and Technological Enterprise (CREATE) Programme—Singapore Peking University Research Centre for a Sustainable Low-Carbon Future, as well as the NTU-A*Star Silicon Technologies Centre of Excellence under program grant no. 112 351 0003. We thank Dr. A. K. Mandal and Dr. S. K. Maji for their assistance during the synthesis and characterization. We are grateful to Dr. Tingchao He for his assistance during the fluorescence measurements. We thank www.designs4research.com for the graphical representation.

REFERENCES AND NOTES

1. Bell, A. G. On the Production and Reproduction of Sound by Light. *Am. J. Sci.* **1880**, *20*, 305–324.
2. Wang, L. V.; Hu, S. Photoacoustic Tomography: *In Vivo* Imaging from Organelles to Organs. *Science* **2012**, *335*, 1458–1462.
3. Ntziachristos, V.; Ripoll, J.; Wang, L. V.; Weissleder, R. Looking and Listening to Light: The Evolution of Whole Body Photonic Imaging. *Nat. Biotechnol.* **2005**, *23*, 313–320.
4. Ntziachristos, V. Fluorescence Molecular Imaging. *Annu. Rev. Biomed. Eng.* **2006**, *8*, 1–33.
5. Liu, T.; Shi, S.; Liang, C.; Shen, S.; Cheng, L.; Wang, C.; Song, X.; Geol, S.; Barnhart, T. E.; Cai, W.; *et al.* Iron Oxide Decorated MoS_2 Nanosheets with Double PEGylation for Chelator-Free Radiolabeling and Multimodal Imaging Guided Photothermal Therapy. *ACS Nano* **2015**, *9*, 950–960.
6. Judenhofer, M. S.; Wehrl, H. F.; Newport, D. F.; Catana, C.; Siegel, S. B.; Becker, M.; Thielscher, A.; Knelling, M.; Lichy, M. P.; Eichner, M. Simultaneous PET-MRI: A New Approach for Functional and Morphological Imaging. *Nat. Med.* **2008**, *14*, 459–465.
7. Sreejith, S.; Joseph, J.; Nguyen, K. T.; Murukeshan, V. M.; Lye, S. W.; Zhao, Y. Graphene Oxide Wrapping of Gold-Silica Core-Shell Nanohybrids for Photoacoustic Signal Generation and Bimodal Imaging. *ChemNanoMat* **2015**, *1*, 39–45.
8. Alfano, R. R.; Demos, S. G.; Gayen, S. K. Advances in Optical Imaging of Biomedical Media. *Ann. N.Y. Acad. Sci.* **1997**, *820*, 248–270.
9. Pysz, M. A.; Gambhir, S. S.; Willmann, J. K. Molecular Imaging Current Status and Emerging Strategies. *Clin. Radiol.* **2010**, *65*, 500–516.
10. Nguyen, K. T.; Sreejith, S.; Joseph, J.; He, T.; Borah, P.; Guan, E. Y.; Lye, S. W.; Sun, H.; Zhao, Y. Poly(Acrylic Acid)-Capped and Dye-Loaded Graphene Oxide-Mesoporous Silica: A Nano-Sandwich for Two-Photon and Photoacoustic Dual-Mode Imaging. *Part. Part. Syst. Charact.* **2014**, *31*, 1060–1066.
11. Maji, S. K.; Sreejith, S.; Joseph, J.; Lin, M.; He, T.; Tong, Y.; Sun, H.; Yu, S. W.-K.; Zhao, Y. Upconversion Nanoparticles as a Contrast Agent for Photoacoustic Imaging in Live Mice. *Adv. Mater.* **2014**, *26*, 5633–5638.
12. Sreejith, S.; Huong, T. T. M.; Borah, P.; Zhao, Y. Organic-Inorganic Nanohybrids for Fluorescence, Photoacoustic and Raman Bioimaging. *Sci. Bull.* **2015**, *60*, 665–678.
13. Sevick-Muraca, E. M.; Houston, J. P.; Gurfinkel, M. Fluorescence-Enhanced, Near Infrared Diagnostic Imaging with Contrast Agents. *Curr. Opin. Chem. Biol.* **2002**, *6*, 642–650.
14. Frangioni, J. V. *In Vivo* Near-Infrared Fluorescence Imaging. *Curr. Opin. Chem. Biol.* **2003**, *7*, 626–634.
15. Yen, S. K.; Jańczewski, D.; Lakshmi, J. L.; Dolmanan, S. B.; Tripathy, S.; Ho, V. H. B.; Vijayaraghavan, V.; Hariharan, A.; Padmanabhan, P.; Bhakoo, K. K.; *et al.* Design and Synthesis of Polymer-Functionalized NIR Fluorescent Dyes-Magnetic Nanoparticles for Bioimaging. *ACS Nano* **2013**, *7*, 6796–6805.
16. Luo, S.; Zhang, E.; Su, Y.; Cheng, T.; Shi, C. A Review of NIR Dyes in Cancer Targeting and Imaging. *Biomaterials* **2011**, *32*, 7127–7138.
17. Zhang, Z.; Wang, J.; Chen, C. Near-Infrared Light-Mediated Nanoplatforms for Cancer Thermo-Chemotherapy and Optical Imaging. *Adv. Mater.* **2013**, *25*, 3869–3880.
18. Ajayaghosh, A. Chemistry of Squaraine-Derived Materials: Near-IR Dyes, Low Band Gap Systems, and Cation Sensors. *Acc. Chem. Res.* **2005**, *38*, 449–459.

19. Sreejith, S.; Carol, P.; Chithra, P.; Ajayaghosh, A. Squaraine Dyes: A Mine of Molecular Materials. *J. Mater. Chem.* **2008**, *18*, 264–274.
20. Baverina, L.; Salice, P. Squaraine Compounds: Tailored Design and Synthesis Towards a Variety of Material Science Applications. *Eur. J. Org. Chem.* **2010**, 1207–1225.
21. Hu, L.; Yan, Z.; Xu, H. Advances in Synthesis and Application of Near-Infrared Absorbing Squaraine Dyes. *RSC Adv.* **2013**, *3*, 7667–7676.
22. Beverina, L.; Sassi, M. Twists and Turns around a Square: The Many Faces of Squaraines Chemistry. *Synlett* **2014**, *25*, 477–490.
23. Chen, H.; Farahat, M. S.; L, K.-Y.; Whitten, D. G. Aggregation of Surfactant Squaraine Dyes in Aqueous Solution and Microheterogeneous Media: Correlation of Aggregation Behavior with Molecular Structure. *J. Am. Chem. Soc.* **1996**, *118*, 2584–2594.
24. Arunkumar, E.; Forbes, C. C.; Noll, B. C.; Smith, B. D. Squaraine-Derived Rotaxanes: Sterically Protected Fluorescence Near-IR Dyes. *J. Am. Chem. Soc.* **2005**, *127*, 3288–3289.
25. Sreejith, S.; Ma, X.; Zhao, Y. Graphene Oxide Wrapping on Squaraine-Loaded Mesoporous Silica Nanoparticles for Bioimaging. *J. Am. Chem. Soc.* **2012**, *134*, 17346–17349.
26. Anees, P.; Sreejith, S.; Ajayaghosh, A. Self-Assembled Near Infrared Dye Nanoparticles as a Selective Protein Sensor by Activation of a Dormant Fluorophore. *J. Am. Chem. Soc.* **2014**, *136*, 13233–13239.
27. Mayerhöffer, U.; Fimmel, B.; Würthner, F. Bright Near-Infrared Fluorophores Based on Squaraines by Unexpected Halogen Effects. *Angew. Chem., Int. Ed.* **2012**, *51*, 164–167.
28. Mayerhöffer, U.; Würthner, F. Halogen-Arene Interactions Assist in Self-Assembly of Dyes. *Angew. Chem., Int. Ed.* **2012**, *51*, 5615–5619.
29. Gao, F.-P.; Lin, Y.-X.; Li, L.-L.; Mayerhöffer, U.; Spenst, P.; Su, J.-G.; Li, J.-Y.; Würthner, F.; Wang, H. Supramoleclular Adducts of Squaraine and Protein for Noninvasive Tumor Imaging and Photothermal Therapy in Vivo. *Biomaterials* **2014**, *35*, 1004–1014.
30. Ahn, H.-Y.; Yao, S.; Wang, X.; Belfield, K. D. Near-Infrared-Emitting Squaraine Dyes with High 2PA Cross-Sections for Multiphoton Fluorescence Imaging. *ACS Appl. Mater. Interfaces* **2012**, *4*, 2847–2854.
31. Volkova, K. D.; Kovalska, V. B.; Tatarets, A. L.; Patsenker, L. D.; Kryvorotenko, D. V.; Yarmoluk, S. M. Spectroscopic Study of Squaraines as Protein-Sensitive Fluorescent Dyes. *Dyes Pigm.* **2007**, *72*, 285–292.
32. Batrakova, E. V.; Kadanov, A. V. Pluronic Block Copolymers: Evolution of Drug Delivery Concept from Inert Nanocarriers to Biological Response Modifiers. *J. Controlled Release* **2008**, *130*, 98–106.
33. Andrade, C. D.; Yanez, C. Q.; Qaggoura, M. A.; Wang, X.; Arnett, C. L.; Coombs, S. A.; Yu, J.; Bassiouni, R.; Bondar, M. V.; Belfield, K. D. Two-Photon Fluorescence Lysosomal Bioimaging with a Micelle-Encapsulated Fluorescent Probe. *J. Fluoresc.* **2011**, *21*, 1223–1230.
34. Akash, M. S.; Rehman, K.; Chen, S. Pluoronic F127-Based Thermosensitive Gels for Delivery of Therapeutic Proteins and Peptides. *Polym. Rev.* **2014**, *54*, 573–597.
35. Bromberg, L. Properties of Aqueous Solutions and Gels of Poly(Ethylene Oxide)-b-Poly(Propylene Oxide)-b-Poly-(Ethylene Oxide)-g-Poly(Acrylic Acid). *J. Phys. Chem. B* **1998**, *102*, 10736–10744.
36. Kabanov, A.; Alakhov, V. Pluoronic Block Copolymers in Drug Delivery: From Micellar Nanocontainers to Biological Response Modifiers. *Crit. Rev. Ther. Drug Carrier Syst.* **2002**, *19*, 1–72.
37. Ros-Lis, J. V.; Garcýá, B.; Jiménez, D.; Martínez-Máñez, R. Squaraines as Fluoro-Chromogenic Probes for Thiol-Contining Compounds and Their Application to the Detection of Biorelevent Thiols. *J. Am. Chem. Soc.* **2004**, *126*, 4064–4065.
38. Sreejith, S.; Divya, K. P.; Ajayaghosh, A. A Near-Infrared Squaraine Dye as a Latent Ratiometric Fluorophore for the Detection of Aminothiol Content in Blood Plasma. *Angew. Chem., Int. Ed.* **2008**, *47*, 7883–7887.